StatSTEM : an efficient approach for accurate and precise model-based quantification of atomic resolution electron microscopy images

StatSTEM: An efficient approach for accurate and precise model-based quantification of atomic resolution electron microscopy images

A. De Backer[a,1], K.H.W. van den Bos[a,1], W. Van den Broek[b], J. Sijbers[c], S. Van Aert[a,*]

[a] *Electron Microscopy for Materials Science (EMAT), University of Antwerp, Groenenborgerlaan 171, 2020 Antwerp, Belgium*
[b] *AG Strukturforschung / Elektronenmikroskopie, Institut für Physik, Humboldt-Universität zu Berlin, Newtonstraße 15, 12489 Berlin, Germany*
[c] *iMinds-Vision Lab, University of Antwerp, Universiteitsplein 1, 2610 Wilrijk, Belgium*

Abstract

An efficient model-based estimation algorithm is introduced to quantify the atomic column positions and intensities from atomic resolution (scanning) transmission electron microscopy ((S)TEM) images. This algorithm uses the least squares estimator on image segments containing individual columns fully accounting for overlap between neighbouring columns, enabling the analysis of a large field of view. For this algorithm, the accuracy and precision with which measurements for the atomic column positions and scattering cross-sections from annular dark field (ADF) STEM images can be estimated, has been investigated. The highest attainable precision is reached even for low dose images. Furthermore, the advantages of the model-based approach taking into account overlap between neighbouring columns are highlighted. This is done for the estimation of the distance between two neighbouring columns as a function of their distance and for the estimation of the scattering cross-section which is compared to the integrated intensity from a Voronoi cell. To provide end-users this well-established quantification method, a user friendly program, StatSTEM, is developed which is freely available under a GNU public license.

Keywords: High-resolution (scanning) transmission electron microscopy (HR (S)TEM), Data processing/image processing, Quantitative electron microscopy, General methods in microscopy, Statistical parameter estimation theory, Tools, Model-based fitting

1. Introduction

Nowadays, more and more quantitative measurements for the analysis of nanomaterials are required. This includes for example locating atomic column positions with a precision in the picometre range, a precise determination of the chemical composition of materials, and counting the number of atoms with single atom sensitivity. Therefore, statistical analysis methods are introduced in order to extract these quantitative measurements from atomic resolution (scanning) transmission electron microscopy ((S)TEM) images. Using statistical parameter estimation theory, unknown structure parameters can be measured with high accuracy and precision from experimental images [1, 2]. This methodology is nowadays becoming recognised as the optimal method for quantitative electron microscopy. In this theory, the (S)TEM image is considered as a data plane from which the unknown structure parameters need to be estimated. The starting point is the availability of a parametric model describing the expectations of the experimental measurements. For atomic resolution (S)TEM images, the projected atomic columns are peaked at the atomic column positions and can be modelled as a superposition of Gaussian functions [3, 4]. The unknown parameters are estimated by fitting this model to the experimental images using a criterion of goodness of fit, quantifying the similarity between the experimental images and the model. For this purpose, the least squares estimator is used in an iterative optimisation scheme. In [2, 5–12], quantitative analyses have successfully been applied for two-dimensional (2D) atomic column position measurements with a precision in the picometre range from TEM images or reconstructed exit waves. More recently, annular dark field (ADF) STEM has also become an important technique for locating 2D atomic column positions [13–16] and quantifying image intensities for composition determination or atom-counting [17–23].

Moreover, one is interested in a quantitative analysis of a larger field of view preserving the highest possible precision and accuracy. Therefore, in this paper, the implementation of the least squares estimator will be reviewed. A direct implementation of this estimator in which all parameters are estimated at the same time is computationally very intensive and is only feasible for images containing a limited number of projected atomic columns in the (S)TEM images, i.e. a limited field of view. A more efficient algorithm is proposed which enables us to analyse large fields of view. The basic idea of the new algorithm is the segmentation of the image into smaller sections containing individual columns without ignoring overlap between neighbouring columns. In this way, only the parameters corresponding to a single atomic column are estimated at the same time, instead of all parameters of the parametric model. In addition, a user friendly software package, called StatSTEM, that includes

*Corresponding author
Email address: sandra.vanaert@uantwerpen.be (S. Van Aert)
[1] Both authors contributed equally to this work.

the algorithm is presented making advanced image quantification using model-based fitting accessible. The program is freely available under a GNU public license, which means briefly that the user is free to use, distribute and alter the program under certain conditions [24].

The algorithm which will be presented here, has already been applied showing that the analysis of larger fields of view opens up a variety of new possibilities for the characterisation of nanomaterials. One of the first applications of this efficient algorithm was the estimation of models for 2D ADF STEM projection images of a bimetallic nanocrystal as an input for electron tomography. Several 2D projection images can be combined into a three-dimensional (3D) reconstruction using a mathematical algorithm to characterise the structure and composition in 3D. By using the fitted models, the influence of noise and scanning distortions could be minimised, revealing the atomic structure in 3D including information about the atom type of each reconstructed atom for the first time [25]. A second example is the analysis of the distribution of the lattice strain in a Au nanodecahedron containing more than 90 000 atoms. Using the efficient model estimation algorithm, it was possible to evaluate the strain distribution in an ADF STEM projection image. This 2D strain distribution could then be compared with the full 3D characterisation of the lattice strain [26]. Very recently, the efficient algorithm has been applied to unscramble mixed elements atom per atom in a Au@Ag core-shell nanorod. For this nanorod, counting results for the Ag and Au atoms have been presented on an absolute scale determining the 3D shape of this heterogeneous nanocrystal from ADF STEM images taken from only two different viewing directions [27].

In order to elucidate the benefits of the model-based fitting in a statistical manner, the accuracy and the precision of the estimated model parameters will be evaluated and the advantages of a model-based approach taking overlap between neighbouring columns into account will be illustrated in this article. These analyses will be performed for ADF STEM imaging, since ADF STEM has become a popular technique for quantitative structure characterisation, such as composition determination and atom-counting, as illustrated by the examples discussed above. For these applications, it is necessary that atomic column positions and total intensities of electrons scattered by the atomic columns, the so-called scattering cross-sections, are estimated unbiasedly with the highest possible precision. Furthermore, it should be noted that the observations for ADF STEM are counting events, which are modelled as Poisson distributed variables. In practice, the estimates of the unknown parameters of the expectation model are obtained using the well-known least squares estimator, which is identical to the maximum likelihood estimator for independent and identically normally distributed pixel values. However, this assumption about the statistical distribution of the pixel values is not always valid, especially not at low electron doses, needed to avoid radiation damage in beam sensitive matter. It will be investigated whether the variance of the least squares estimates of scattering cross-sections and atomic column positions attains the theoretical lower bound on the variance of the estimated parameters. This study reveals if a quantitative analysis would benefit when applying the maximum likelihood estimator which has optimal statistical properties. Moreover, a comparison with an approach ignoring the overlap between neighbouring columns is made to illustrate the effect on the estimated column positions and scattering cross-sections. Currently, two approaches exist to measure scattering cross-sections: by using the volumes under a Gaussian peak [17–23] or by integrating the image contribution of each atomic column [28–31]. In the second case, use is made of so-called Voronoi cells, in which each pixel is assigned to the nearest atomic column. In order to compare both approaches, the effect of overlap between neighbouring columns on the estimated values is investigated.

The article is organised as follows. In section 2, the principles of model-based parameter estimation will be reviewed. In section 3, the efficient algorithm for the estimation of atomic column positions and intensities from HR(S)TEM images will be introduced. The accuracy and the precision of the estimated parameters will be discussed in section 4. Next, the advantages of using a model-based approach taking into account overlap between neighbouring columns will be illustrated in section 5. In section 6, StatSTEM, a user friendly program for image quantification will be presented. Finally, in section 7, conclusions will be drawn.

2. Model-based parameter estimation

High-resolution (S)TEM images do not directly provide quantitative measurements of the unknown structure parameters, such as atomic column positions, peak intensities, and scattering cross-sections. Therefore, these images are used as a starting point for the measurement of structure parameters using statistical parameter estimation theory. In this way, it becomes possible to determine structure parameters with a precision that is orders of magnitude better than the resolution of the electron microscope. This requires a quantitative model-based method, in which the observed (S)TEM image is considered as a data plane from which unknown structure parameters have to be estimated in a statistical way. For a successful application, a parametric model describing the expectations of the pixel values in the high resolution (HR) (S)TEM image should be available.

For HR(S)TEM images, the intensity is often sharply peaked at the atomic column positions [3, 4]. Therefore, HR(S)TEM images are often modelled as a superposition of Gaussian peaks. The expectation of the intensity of pixel (k, l) at position (x_k, y_l) can then be described by an expectation model $f_{kl}(\boldsymbol{\theta})$, with $\boldsymbol{\theta}$ the vector of unknown structure parameters, as:

$$f_{kl}(\boldsymbol{\theta}) = \zeta + \sum_{i=1}^{I} \sum_{m_i}^{M_i} \eta_{m_i} \exp\left(-\frac{\left(x_k - \beta_{x_{m_i}}\right)^2 + \left(y_l - \beta_{y_{m_i}}\right)^2}{2\rho_i^2} \right) \quad (1)$$

with ζ a constant background, ρ_i the column dependent width of the Gaussian peak, η_{m_i} the column intensity of the m_ith Gaussian peak, $\beta_{x_{m_i}}$ and $\beta_{y_{m_i}}$ the x- and y-coordinate of the m_ith atomic column respectively. The index i refers to atomic columns of the same atom type with I different types and the index m_i refers to the mth column of type i with M_i the number of

columns of type i. The indices in the summation of Eq. (1) can be simplified in the case of a mono-type crystalline nanostructure since then only one column type is present. The unknown parameter of the parametric imaging model of Eq. (1) are given by the parameter vector $\boldsymbol{\theta}$:

$$\boldsymbol{\theta} = \left(\beta_{x_{1_1}}, \ldots, \beta_{x_{M_I}}, \beta_{y_{1_1}}, \ldots, \beta_{y_{M_I}}, \rho_1, \ldots, \rho_I, \eta_{1_1}, \ldots, \eta_{M_I}, \zeta\right)^T. \tag{2}$$

For ADF STEM, the volume under a peak above a background reflects the total intensity of electrons scattered toward the ADF detector for every atomic column. This is the so-called scattering cross-section which can be used to quantify chemical composition or number of atoms in a projected atomic column from an ADF STEM image. The scattering cross-section V_{m_i} of the m_ith Gaussian peak can be calculated from the model parameters, the width ρ_i and the height η_{m_i}, as follows [17]:

$$V_{m_i} = 2\pi\eta_{m_i}\rho_i^2. \tag{3}$$

The proposed theoretical parametric model should describe the image intensities accurately in order to extract reliable quantitative measurements from HR(S)TEM images. This simplified empirical model, which consists of a superposition of Gaussian peaks as described by Eq. (1), is not necessarily less suitable than more complicated models. Complicated models describe the image intensities in detail using a more physics-based approach, i.e. modelling the electron-object interaction and the transfer of the electrons through the microscope. However, the number of unknown parameters will be higher for such models, e.g. unknown microscope parameters should then be included in the parametric model. A higher number of unknown parameters has the disadvantage that the optimisation might end up in a local minimum, if appropriate starting values for the unknown parameters are not available. Therefore, the lower number of parameters of the simpler model given by Eq. (1) has its benefit. In addition, structure parameters of interest, such as atomic column positions and scattering cross-sections, are accounted for by the simpler model. The validity of the proposed model, given by Eq. (1), has been shown for high resolution TEM images using different statistical model assessment methods, such as the likelihood ratio test [1, 2]. For high resolution STEM images, the validity of the model will be shown in terms of accuracy and precision of the estimated structure parameters in Sections 4 and 5.

The parametric model of Eq. (1) is fitted to the experimental data using the uniformly weighted least squares criterion quantifying the similarity between the experimental images and the model. The uniformly weighted least squares estimates $\hat{\boldsymbol{\theta}}$ of the unknown parameters $\boldsymbol{\theta}$ are then given by the values of $\mathbf{t}$ that minimise the uniformly weighted least squares criterion:

$$\hat{\boldsymbol{\theta}} = \arg\min_{\mathbf{t}} \sum_{k=1}^{K}\sum_{l=1}^{L} (w_{kl} - f_{kl}(\mathbf{t}))^2 \tag{4}$$

where w_{kl} corresponds to the observed pixel value in a HR(S)TEM image at position (k, l), with K and L the number of pixels in x- and y-direction, respectively. Direct implementation of the least squares estimator as described by Eq. (4), in which all parameters are estimated at the same time, is computationally very intensive and only feasible for images containing a limited number of projected atomic columns. Therefore, in Section 3, a more efficient algorithm is proposed for obtaining estimates of the unknown structure parameters.

3. Efficient model estimation algorithm

In this section, an efficient model estimation method for the analysis of atomic resolution (S)TEM images including images with a large field of view will be described. The general idea behind this method has been proposed in [32]. The model estimation algorithm has now further been improved and extended. As compared to the scheme presented in [32], the starting values for the width of the Gaussian peaks and the estimation of the height of the Gaussian peaks and the background within the iterative part have now been optimised. More important, a new estimation scheme has been added allowing to estimate the same width for estimated Gaussian peaks of atomic columns of the same atom type. In addition, a software package, StatSTEM, including this algorithm is developed.

The parametric model that is implemented is the superposition of Gaussian peaks describing the peaked intensity at the atomic column positions as described by Eq. (1) in the previous section. The idea of the new algorithm is a segmentation of the image into smaller sections containing individual atomic columns without ignoring overlap between neighbouring columns. Therefore, it is required that the image can be described as a superposition of the individual atomic columns. For example, incoherent imaging in ADF STEM meets this necessary condition.

Two different schemes for the model estimation are proposed for two different variants of the parametric models describing (S)TEM images. In the first model, each atomic column is modelled with a different width for the Gaussian peak; this model estimation scheme will be referred to as 'model estimation A'. In the second model, the same width is imposed for atomic columns of the same atom type; this model estimation scheme will be referred to as 'model estimation B'. Different widths for each Gaussian in the parametric model corresponding to the intensity of an atomic column in the (S)TEM image, as in 'model estimation A', are required if no prior knowledge is available on for example the atomic column types. However, if prior knowledge is available, the number of parameters of the expectation model that needs to be estimated in the model can be reduced, as in 'model estimation B'. This approach enhances the precision of the parameter estimates. In addition, the estimation of the parameters of such a model will be more robust in the case of the inevitable presence of different types of noise (e.g. scanning noise in STEM images), since less parameters need to be estimated in this model. The estimates for the parameters for 'model estimation A' do often not converge because of noise.

In subsection 3.1, 'model estimation A' with a different width assumed for each Gaussian is introduced. Next, subsection 3.2

introduces 'model estimation B' where the same width is assumed for Gaussian peaks of the atomic columns of the same atom type.

3.1. Model estimation A

Different width for each estimated Gaussian peak of an atomic column

When a different width is assumed for each estimated Gaussian corresponding to the intensity of an atomic column, the parametric model $f_{kl}(\boldsymbol{\theta})$ for the intensity of pixel (k, l) at position (x_k, y_l) is given by:

$$f_{kl}(\boldsymbol{\theta}) = \zeta + \sum_{n=1}^{N} \eta_n \exp\left(-\frac{(x_k - \beta_{x_n})^2 + \left(y_l - \beta_{y_n}\right)^2}{2\rho_n^2}\right) \quad (5)$$

with ζ a constant background, ρ_n and η_n the width and height of the nth Gaussian peak, β_{x_n} and β_{y_n}, the x- and y-coordinate of the nth atomic column respectively, and N the total number of atomic columns. The unknown parameters $\boldsymbol{\theta}$ of the expectation model are then given by:

$$\boldsymbol{\theta} = \left(\beta_{x_1}, \ldots, \beta_{x_N}, \beta_{y_1}, \ldots, \beta_{y_N}, \rho_1, \ldots, \rho_N, \eta_1, \ldots, \eta_N, \zeta\right)^T. \quad (6)$$

It is assumed that proper starting values are available for the parameters of the empirical model. Good starting values are necessary in order to avoid ending up in a local minimum during the model estimation procedure. Initial values for the widths ρ_n of the Gaussian peaks are easy to provide and starting coordinates for the positions β_{x_n} and β_{y_n} of projected atomic columns can be given using a peak finding routine. For this purpose, the image resolution should be high enough. This means that a high-resolution image is required, where individual columns are atomically resolved. If the resolution is only just sufficient, prior knowledge on the structure, e.g. the presence of dumbbells, can still provide the starting values for atomic column positions.

The parametric model given by Eq. (5) is linear in the parameters for the height of the Gaussian peaks η_n and the background ζ and is non-linear in the parameters for the positions β_{x_n}, β_{y_n}, and the width of the Gaussian peaks ρ_n. The parameters β_{x_n}, β_{y_n}, and ρ_n are therefore the non-linear parameters of the model and will be denoted as the vector $\boldsymbol{\alpha}$. An initial guess for the linear parameters of the model, i.e. the heights η_n and background ζ denoted as the vector $\boldsymbol{\xi}$, is not needed, since the linear parameters in the model can be replaced by their linear least squares estimates given the values of the non-linear parameters of the model [33]. These linear least squares estimates are the best companion values for the linear parameters and the computation involves only a simple linear regression. In addition, this approach has a second benefit apart from the fact that no starting guesses are needed for the linear parameters. The number of parameters that needs to be estimated in an iterative procedure is reduced to the non-linear parameters only, increasing the convergence speed of the model estimation.

Schematically, the proposed algorithm for model estimation is outlined in Fig. 1. In the first steps (B.) and (C.), initial guesses are obtained for the non-linear parameters $\boldsymbol{\alpha}_1$ for the input image (A.). In step (B.), initial guesses for the x- and y-coordinates of the atomic columns in the image are obtained by a peak finding routine. Next, using these starting coordinates and a rough starting estimate for the width ρ based on the distance between the atomic columns, the starting value for the width is refined in step (C.) using the full image containing all the atomic columns. For this purpose, a derivative-free unconstrained non-linear optimisation method, the Nelder-Mead simplex method, is used in order to reduce the memory consumption [34]. If a limited number of parameters needs to be estimated, than this method converges toward good estimates for the parameters. Here, a single starting value for the width of all atomic columns is estimated. For the estimation of this refined starting value for the width, the tolerance level of the Nelder-Mead simplex algorithm is set less tight. Next, the iterative part of the fitting procedure can be executed (shown in grey in Fig. 1). Based on the values of the non-linear parameters $\boldsymbol{\alpha}_j$, starting values for the linear parameters $\boldsymbol{\xi}_j$ are calculated by means of linear regression (D.), where j corresponds to the number of the iterations. Having starting values for the linear and non-linear parameter of the jth iteration available (E.), the actual estimation of the parameters can be done. Therefore, regions of interest containing single atomic columns are selected from the HR(S)TEM image (F.). The regions are defined based on the average distance between the atomic columns in the image. These distances can be calculated from the coordinates given by the peak finding routine. Next, the parameters of the neighbouring projected atomic columns are selected (G.) in order to take overlap between neighbouring Gaussian shapes into account. The values of the non-linear and linear parameters are given by the values that result from step (B.), (C.), and (D.) in the first iteration and by the values that resulted from step (O.) and (D.) in further iterations. The contributions of these neighbouring Gaussian peaks in the region of interest of the single atomic column are calculated (H.). Then, these contributions are subtracted from the image of the single atomic column (I.). Ideally, the thus obtained image only contains scattered intensities resulting from this single projected atomic column and can be used for a non-linear least squares estimation of the non-linear parameters of this single Gaussian (J.). Steps (F.) till (J.) are repeated for each projected atomic column in the HR(S)TEM image in order to obtain a complete set of estimated non-linear parameters $\hat{\boldsymbol{\alpha}}_j$ for the jth iteration. Next, the best companion values for the linear parameters for the jth iteration, $\hat{\boldsymbol{\xi}}_j$ are calculated (K.). Once the parameters are estimated, convergence is evaluated (M.). If convergence is not yet obtained, the non-linear starting values for the $(j+1)$th iteration are calculated based on the starting and estimated values for the non-linear parameters of the jth iteration (O.). Here, the updates are modified by a scaling factor ν in order to avoid divergence on the parameters to be estimated. Having a new set of non-linear parameters available, the iterative part of the fitting algorithm can be executed again from step (D.). The iterative approach allows a better modelling of the overlap between neighbouring Gaussian peaks. If convergence is attained (P.), the model can be calculated based on the estimated parameters (Q.).

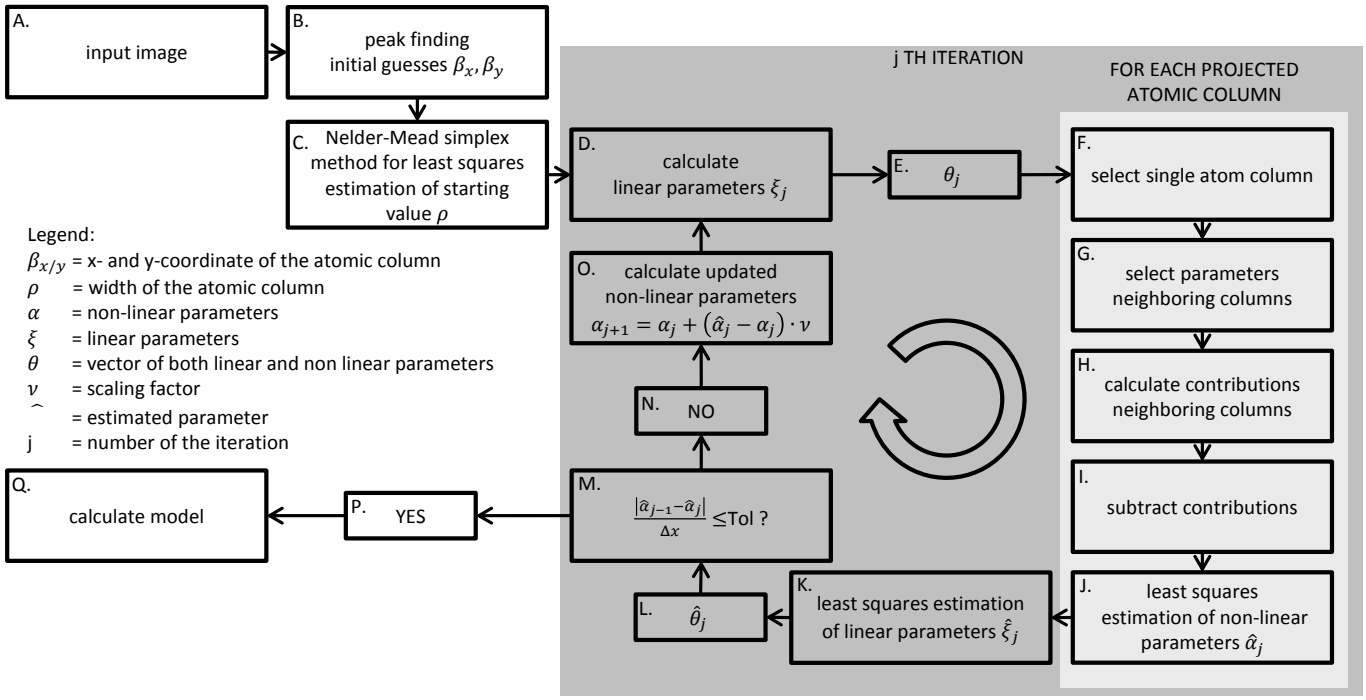

Figure 1: Schematic for model estimation A: algorithm for the expectation model having a different width for each estimated Gaussian peak.

3.2. Model estimation B

Same width assumed for estimated Gaussian peaks of atomic columns of the same atom type

When the same width is estimated for Gaussian peaks of atomic columns of the same atom type, the expectation model $f_{kl}(\boldsymbol{\theta})$ and corresponding unknown structure parameters $\boldsymbol{\theta}$ are given by Eqs. (1) and (2), which are repeated here:

$$f_{kl}(\boldsymbol{\theta}) = \zeta + \sum_{i=1}^{I} \sum_{m_i}^{M_i} \eta_{m_i} \exp\left(-\frac{\left(x_k - \beta_{x_{m_i}}\right)^2 + \left(y_l - \beta_{y_{m_i}}\right)^2}{2\rho_i^2} \right) \quad (7)$$

with unknown parameters:

$$\boldsymbol{\theta} = \left(\beta_{x_{1_1}}, \ldots, \beta_{x_{M_I}}, \beta_{y_{1_1}}, \ldots, \beta_{y_{M_I}}, \rho_1, \ldots, \rho_I, \eta_1, \ldots, \eta_{M_I}, \zeta\right)^T . \quad (8)$$

The basic idea of this routine is equivalent to the method for the model having different widths for each estimated Gaussian peak. The estimation method is subdivided into the estimation of the position parameters $\beta_{x_{m_i}}$ and $\beta_{y_{m_i}}$, and the estimation of the width ρ_i for each atom type. This approach is valid since the correlation between the position parameters and the width of the Gaussian peaks equals almost zero. Also throughout this estimation routine, the best companion values for the linear parameters $\boldsymbol{\xi}$ are used in each iteration increasing the convergence of the model estimation.

A schematic is shown in Fig. 2. The first steps of model estimation B are similar to steps (A.), (B.), and (C.) of model estimation A. In step (B.), initial guesses are obtained for the coordinates of the projected atomic columns in input image (A.) using a peak finding routine. If different column types are present, the atomic columns are grouped by type. Next, in step (C.), refined initial guesses for the widths of the atomic columns of the same atom type are obtained using the Nelder-Mead simplex method with a less tight tolerance level applied to the full image containing all atomic columns. Since the number of different atom types in a HR(S)TEM image is limited, this method gives also for model estimation B accurate estimates in an efficient manner. Next, the iterative part of model estimation A is performed till convergence is reached (D.) without the estimation of the parameters for the width of the Gaussian peaks, i.e. with a fixed value for the width ρ_i of each atomic column type set in step (C.). In this way, estimates are obtained for the x- and y-coordinates $\beta_{x_{m_i}}$ and $\beta_{y_{m_i}}$ (E.). Next, estimates for the width ρ_i and the companion values for the linear parameters $\boldsymbol{\xi}$ need to be estimated for the fixed positions obtained from the first part of this method. A full optimisation of the parameter ρ_i is done using the Nelder-Mead simplex method with a tight tolerance level applied to the full image containing all atomic columns (F.). After the optimisation of the parameter ρ_i, estimates are available for all the non-linear parameters $\hat{\boldsymbol{\alpha}}$ in the parametric model (G.). Finally, the best companion values for the linear parameters $\hat{\boldsymbol{\xi}}$ (H.) and the model based on the estimated parameters (I. and J.) can be calculated.

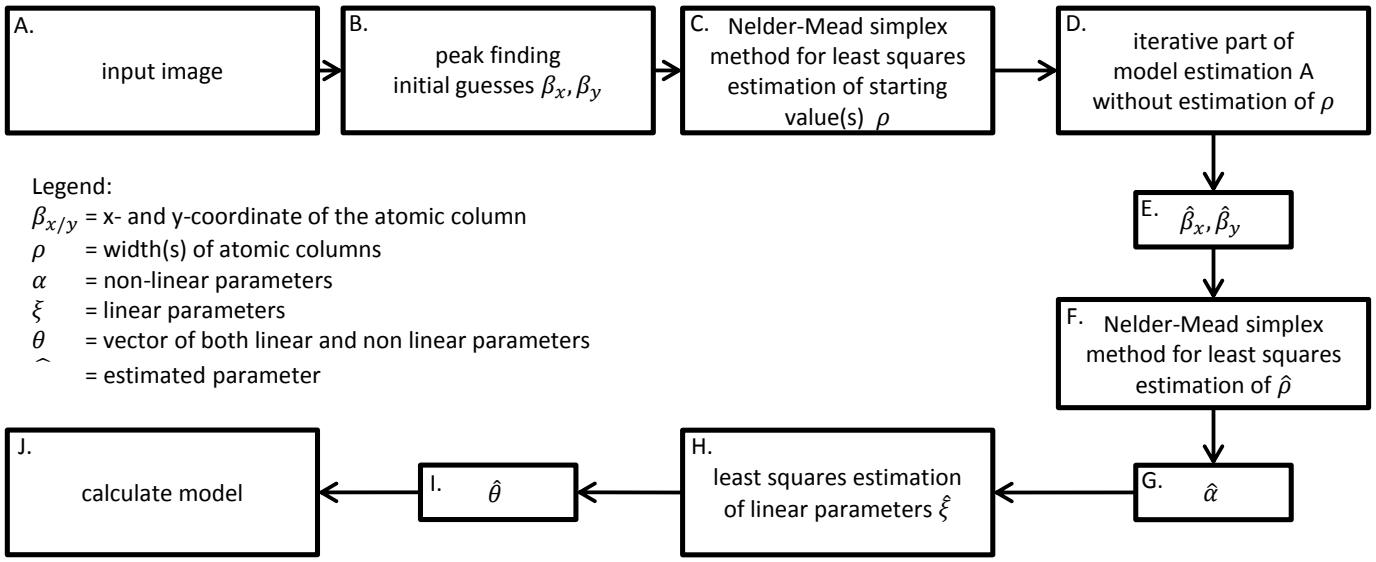

Figure 2: Schematic for model estimation B: algorithm for the expectation model having the same width for Gaussian peaks of atomic columns of the same atom type.

4. Evaluation of the accuracy and precision of the estimated model parameters in ADF STEM

The aim in quantitative electron microscopy is to estimate the structure parameters unbiasedly and as precise as possible. Ultimately, this precision is only limited by the presence of counting noise. Due to noise, the pixel values in the experimental images will fluctuate randomly from experiment to experiment. These pixel values or observations can therefore be modelled as random variables, characterised by a joint probability density function (PDF) (in the case of continuous observations) or a joint probability function (PF) (in the case of discrete observations, such as Poisson counting results). The parametric model introduced in sections 2 and 3 describes the expectations of these observations. Use of the concept of Fisher information allows one to derive an expression for the highest attainable precision with which the structure parameters of the object under study can be estimated in an unbiased way [35]. This expression defines a lower bound on the parameter variance. This bound, which is known as the Cramér-Rao lower bound (CRLB), can be derived from the P(D)F. The CRLB on the variance of the parameters can be attained when applying the maximum likelihood estimator. In the case of identically independent normally distributed variables, the maximum likelihood estimator equals the well known least squares estimator. Since the Poisson distribution tends to be a normal distribution for increasing expectation values for the pixel values, the least squares estimator is often applied. This means that when the detected electron dose is high and if the contrast in the images is low, the uniformly weighted least squares estimator gives maximum likelihood estimates for the unknown parameters. However, this assumption about the statistical distribution of the pixel values is not always valid, especially not at low electron doses, which is often needed to avoid radiation damage in beam-sensitive matter. This would imply that the optimal statistical properties of the maximum likelihood estimator are lost. Therefore, the accuracy and precision of the estimated parameters of interest, i.e. the atomic column position and the scattering cross-section, will be investigated for a higher and lower incident electron dose. In order to evaluate the precision and accuracy, use will be made of detailed ADF STEM multislice simulations. The true values of the parameters will be compared with the sample means in order to verify the accuracy. This will be done for the atomic column positions and scattering cross-sections obtained from different noise realisations of a ADF STEM multislice simulation. The precision will be evaluated by comparing the sample variance with the CRLB. In this manner, it can be examined if all information contained in the images is extracted using a particular estimation procedure, which is here the uniformly weighted least squares estimator as implemented in the efficient model estimation algorithm. In Appendix A, the attainable precision, i.e. the CRLB on the variance, for the position parameters and the scattering cross-sections will be derived in detail.

In subsection 4.1, the ADF STEM simulations will be discussed briefly, before the results of the simulation study for the assessment of the accuracy and precision of the parameters of interest will be shown in subsection 4.2.

4.1. ADF STEM simulation study

The analysis presented here will make use of multislice simulations under the absorptive potential approximation [36], because of its suitability to describe electron-sample interaction for thin samples. The ADF STEM images are calculated using the STEMsim software [37]. The absorptive potential approximation is computationally less demanding while it still describes the image intensities properly up to 50 nm thickness of the sample [38]. We simulated a Pt structure in [100] zone

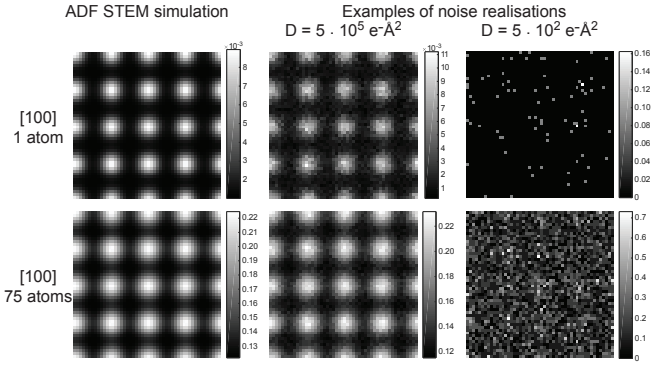

Figure 3: Central part of detailed ADF STEM simulations for [100] orientation for 1 atoms and 75 atoms thickness. Examples of the corresponding normalised noise realisations for an incoming electron dose of $N_d = 5 \cdot 10^2$ e^-Å^{-2} and $N_d = 5 \cdot 10^5$ e^-Å^{-2} are also shown.

axis up to 75 atoms thickness, i.e. $\approx$ 30 nm. The simulated images were convolved with a Gaussian function to account for spatial incoherence. The simulation settings are summarised in Table 1. The Debye-Waller factor in the table describes the atomic vibrations. This Debye-Waller factor is temperature dependent and has been parametrised for several elemental crystals and compounds with zinc-blende structure in [39].

Model estimation B has been used to estimate the scattering cross-sections and atomic column positions from the simulated images. As presented in [20], fitting a constant background to a simulation is not needed, since the background considers signals that do not originate from the sample under study, such as the sample support or grid. Consequently, a background with value 0 was considered for this analysis.

Parameter	Symbol	Value
Acceleration voltage	V_0 (kV)	300
Defocus	ϵ (nm)	−8.8741
Spherical aberration	C_s (mm)	0.04
Spherical aberration of 5th order	C_5 (mm)	10
Objective aperture angle	α (mrad)	21.1
Spatial incoherence of source	FWHM (Å)	0.7
Number of unit cells per supercell	$N_a \times N_b$	9×9
ADF inner collection angle	β_1 (mrad)	60
ADF outer collection angle	β_2 (mrad)	190
Maximum specimen thickness	$z_{[100]}$ (nm)	29.4
Debye-Waller factor	B (Å^2)	0.384
Pixel size	$\Delta x = \Delta y$ (Å)	0.1569

Table 1: Settings used for absorptive potential multislice simulations of Pt in [100] zone axis.

4.2. Results

It is expected that the lower bound on the variance of the unknown parameters, i.e. the atomic column positions and the scattering cross-sections, can be attained when applying the maximum likelihood estimator and if unbiased estimates are obtained. Here, the least squares estimator is used, although the observations are modelled as independent Poisson distributed variables. Therefore, the attainability of the lower bound on the variance of the atomic column position and the scattering cross-section will be investigated for different incident electron doses. This study allows us to reveal if a quantitative ADF STEM analysis would benefit when applying the maximum likelihood estimator which has optimal statistical properties.

Detailed ADF STEM simulations are available for increasing thickness from 1 to 75 atoms for Pt in the [100] orientation as described in the previous subsection. In order to evaluate the attainability of the CRLB, different values for the incident electron dose N_d (e^-/Å^2) are considered:

$$\lambda_{kl} = N_p h_{kl} = N_d \Delta x \Delta y h_{kl} \tag{9}$$

where λ_{kl} equals the expectation model including the electron dose, h_{kl} equals the detailed ADF STEM simulation, N_p equals the incident electron dose per pixel, $\Delta x = \Delta y$ equals the pixel size, and N_d the incident electron dose per unit area. Atomic resolution imaging is still possible with doses of the order of $N_d = 10^2$ e^-Å^{-2} for LAADF STEM according to [40]. Therefore, electron doses of $N_d = 5 \cdot 10^5$ e^-Å^{-2}, and $N_d = 5 \cdot 10^2$ e^-Å^{-2} are used in the simulation study based on ADF STEM images. For each thickness, 100 noise realisations are simulated for the two different doses. Next, the noise realisations are normalised with respect to the incident electron dose, i.e. divided by the incident electron dose placing the noise realisations on the same intensity scale as the detailed image simulation h_{kl} from STEMsim. The detailed STEM simulation and corresponding noise realisations are illustrated in Fig. 3.

From the noise realisations, the parameters of the parametric model of model estimation B given by Eq. (7) are estimated. For the low dose images, prior knowledge of the presence of the atomic columns has been used. The parameters that are evaluated here are the x-coordinate and the normalised scattering cross-section of the central atomic column in the simulated ADF STEM image. Only the x-coordinate is evaluated since the x- and y-coordinate show exactly the same behaviour for this symmetric simulation. In order to evaluate the accuracy of the estimates, the sample means have been compared with the reference values. For the atomic column positions, the reference value equals the true value of the atomic column position of the input structure of the STEM simulations described in the previous paragraph. For the scattering cross-sections, the estimated values from the detailed ADF STEM simulation h_{kl} (in the absence of Poisson distributed noise) is taken as a reference. The expressions for the confidence intervals on the sample mean and sample variance of the x-coordinate and the scattering cross-section of the central atom are given in Appendix B.

The results of the study of the accuracy of the position coordinates and scattering cross-sections are shown in Fig. 4 for electron doses of $N_d = 5 \cdot 10^5$ e^-Å^{-2} and $N_d = 5 \cdot 10^2$ e^-Å^{-2}, i.e. a higher and lower incident electron dose. The sample means from the estimates resulting from the 100 noise realisations are plotted together with the true values of the x-coordinate and scattering cross-section of the central atomic column. It is clear

that unbiased estimates are obtained for both the x-coordinate as well as the scattering cross-section of the central atomic column. For the higher incident electron dose, the 95% confidence intervals of the scattering cross-sections are too small to be visible in Fig. 4(b). It is clear that the confidence intervals on the sample means become larger when reducing the incident electron dose. The estimates for the x-coordinates and the scattering cross-sections of the central atomic column are still accurate for this lower incident electron dose.

The results for the precision of the estimated position coordinates and scattering cross-sections are shown in Fig. 5 for both electron doses. In these figures, the sample variances from the estimates of the 100 noise realisations are plotted together with the theoretical lower bound on the variance, the CRLB. Two main conclusions can be drawn from this Fig. 5. First, the CRLB allows us to evaluate the precision as a function of the number of atoms for the position coordinates and scattering cross-sections. The variance of the position coordinate of the atomic columns decreases up to 20 atoms. Beyond this thickness, the probe will be delocalised and the variance on the position coordinates increases. The variance on the scattering cross-section increases with increasing number of atoms in a projected atomic column. Second, the attainability of the CRLB can be evaluated from these figures. For the higher incident electron dose in Figs. 5(a) and (b), the CRLB is attained for the whole range of number of atoms. For the reduced electron dose in Figs. 5(c) and (d), the CRLB on the variance of the x-coordinate and scattering cross-sections of the central atomic column is not attained for very small number of atoms. This result is not unexpected since the detected number of electrons is very low in this case. Indeed, with a pixel size of 0.1569 Å for Pt [100], the incident electron dose per pixel equals approximately 12 e^-/pixel. Since the maximal pixel intensity for single atom thickness expressed as a fraction of the incident electron beam equals approximately 0.01, the probability that an electron is detected will be very low. This is also clear from the noise realisations with $N_d = 5 \cdot 10^2$ e^-Å^{-2} in Fig. 3. In this case, the noise realisation does not show the shape of the atomic columns anymore. Because of the prior knowledge of the presence of atomic columns, an attempt to estimate the model parameters is made, although the model estimation starts to fail here. For practical applications requiring the same low incident electron dose, the detected dose per pixel should be increased, which can be done by increasing the pixel size while keeping the same total incident electron dose and/or decreasing the inner angle of the STEM detector. Nevertheless, this simulation study shows that the lower bound on the variance is nearly completely attained for the estimation of the position coordinates and scattering cross-sections from ADF STEM images which are assumed to have independent Poisson distributed pixel values. This result is of great importance, since this means that the parameters of interest are obtained with the highest possible precision when using the uniformly weighted least squares estimator as implemented in the efficient model estimation algorithm. Since the highest possible precision is attained even for low incident electron doses using the least squares estimator, the implementation of the maximum likelihood estimator would have no extra benefit.

5. Advantages of a model-based approach

The quantification of electron microscopy images can be done by either using a direct or a model-based approach. The advantage of a model-based approach is that it allows one to extract structure parameters with an accuracy and precision that is orders of magnitude better than the resolution of the microscope. A direct approach is often computationally less demanding as compared to a model-based approach. For example, atomic column locations can be found by peak finding routines, which search for local maxima in the images [31, 41]. Within the model-based approach, different methods and implementation can be used. An often used approach is to ignore the overlap between neighbouring columns as this enables a fast algorithm that does not require the iterative steps visualised in Fig. 1 [42, 43].

Taking into account overlap can affect significantly not only the estimated column locations, but also the scattering cross-sections. The latter quantity is measured by either estimating the volume under a Gaussian peak or often by integrating the image contributions of each atomic column. For this last approach, use is made of the so-called Voronoi cells [28, 30, 31], in which each pixel is assigned to the nearest atomic column. Furthermore, the Voronoi cell approach is not capable of identifying overlapping intensities of neighbouring atomic columns. In order to illustrate the effect on the estimated parameters when taking the overlap into account, ADF STEM image simulations of a 5-atoms-thick Pt column neighbouring a 3-atoms-thick Pt column with a varying distance between the columns are investigated. Two columns of a different thickness have been used as in practice many nanoparticles do not have a uniform thickness. The smallest distance is set to 0.7 Å as the shortest bond length in nature equals 74 pm, that of the hydrogen molecule. Examples of the ADF STEM image simulations are shown in Fig. 6(a). Multislice simulations have been performed under the absorptive potential approximation [36, 37] with settings as summarised in Table 1 and a pixel size equal to 0.1 Å. The simulated images were convolved with a Gaussian function to account for spatial incoherence.

In subsection 5.1, the advantages of taking the overlap of image intensities into account when estimating the atomic column positions are investigated. Next, subsection 5.2 discusses the influence of overlapping image intensities on the estimated scattering cross-sections.

5.1. Atomic column locations

The overlap of image intensities of neighbouring atomic columns becomes more significant when the distance between the columns decreases. In order to illustrate this, an algorithm ignoring the overlap between neighbouring columns has been used based on the model estimation algorithm presented in subsection 3.2. In Fig. 6(b), the distance between the column obtained from the estimated column locations is shown together

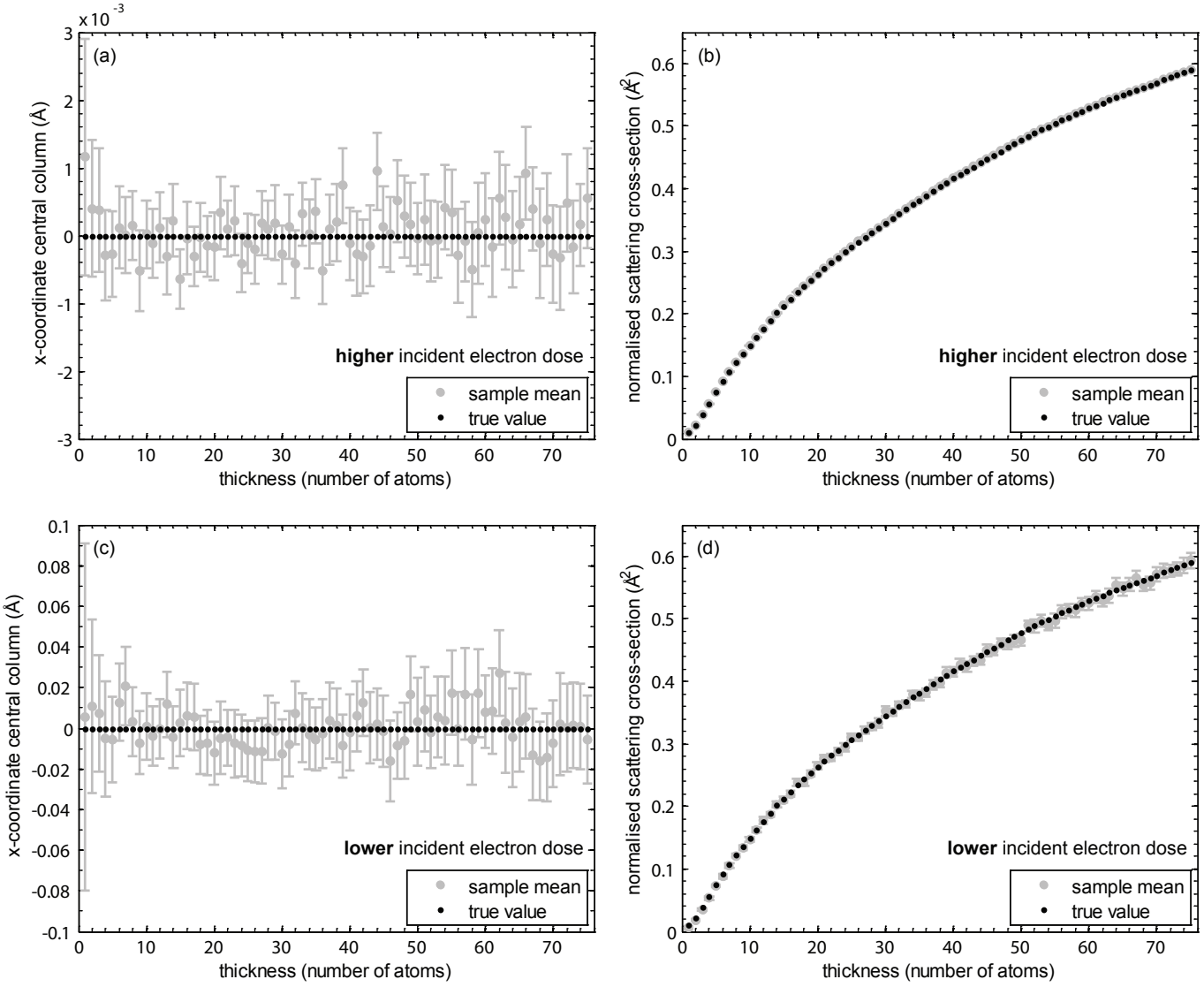

Figure 4: **Accuracy** of the estimated scattering cross-sections and position coordinates for two different incoming electron doses. The true values and the sample mean together with the 95% confidence interval are shown for the (a) x-coordinate of the central atomic column for $N_d = 5 \cdot 10^5$ e^-Å^{-2}, (b) scattering cross-sections for $N_d = 5 \cdot 10^5$ e^-Å^{-2}, (c) x-coordinate of the central atomic column for $N_d = 5 \cdot 10^2$ e^-Å^{-2} , and (d) scattering cross-sections for $N_d = 5 \cdot 10^2$ e^-Å^{-2}.

with the results obtained by the algorithm taking overlap into account. Only above a distance of about 2 Å, the model ignoring the overlap accurately estimates the distance. In comparison, the model which takes the overlap into account is more accurate over the whole range. Here, small deviations only start to occur at distances smaller than 1 Å. In this range, the overlap of intensities makes it hard to resolve the two columns. Because of the prior knowledge of the presence of two atomic columns, an attempt can be made to estimate model parameters. In practice, distances between neighbouring atomic columns are often below 2 Å, making it essential to use an approach in which the overlap is modelled.

5.2. Volumes versus integrated intensities

The used method for quantifying the scattering cross-sections from ADF STEM images can significantly influence the measured values. In this subsection, two measures are compared: volumes [9, 18–22] and integrated intensities from Voronoi cells [28, 30, 31, 44]. For obtaining the scattering cross-sections by using Voronoi cells, atomic column locations have to be known. For experimental images, where atomic column locations are unknown, peak finding routines or model-based approaches can be used. In this study, the exact input coordinates of the atomic column in the simulations are used to define the Voronoi cells in the most accurate manner. The algorithm presented in subsection 3.2 has been used to measure the scattering cross-sections by using the volumes under the Gaussian peak. In Fig. 6(c), the obtained scattering cross-sections for the two columns by both approaches are shown. For a distance larger than 2 Å, both approaches result in approximately the same values. Below this distance, the overlap of image intensities affects the scattering cross-sections measured by the Voronoi cell approach. In this region, the tail of the 5-atoms-thick column in-

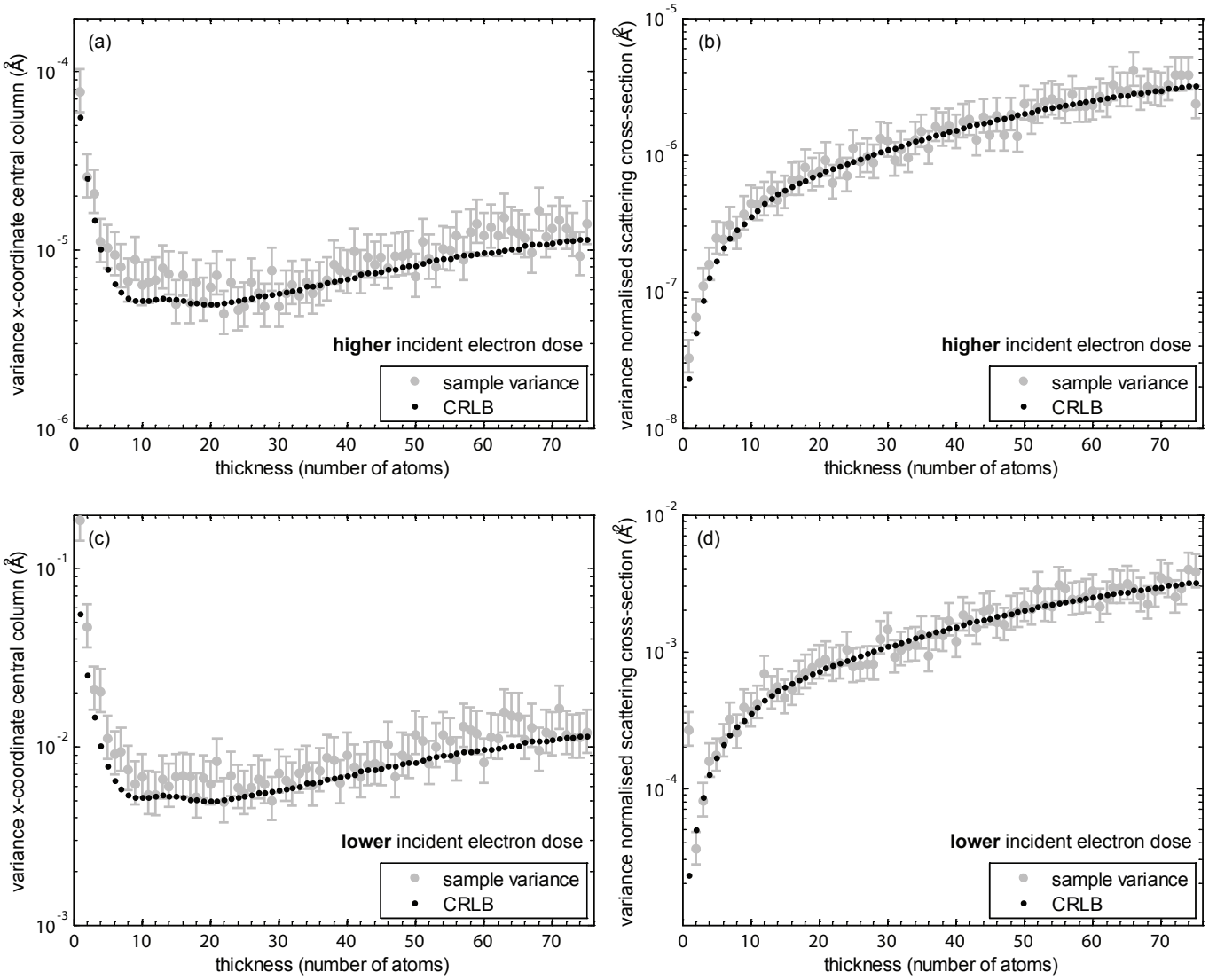

Figure 5: **Precision** of the estimated scattering cross-sections and position coordinates for two different incoming electron doses. The Cramér-Rao lower bound and the sample variances together with the 95% confidence interval are shown for the (a) x-coordinate of the central atomic column for $N_d = 5 \cdot 10^5$ e^-Å^{-2}, (b) scattering cross-sections for $N_d = 5 \cdot 10^5$ e^-Å^{-2}, (c) x-coordinate of the central atomic column for $N_d = 5 \cdot 10^2$ e^-Å^{-2}, and (d) scattering cross-sections for $N_d = 5 \cdot 10^2$ e^-Å^{-2}.

creases the image intensities around the 3-atom-thick column. The Voronoi cell approach is not capable to compensate for this effect. The estimated scattering cross-sections by the Gaussian volumes remain approximately constant over the entire range. Small fluctuations can be explained by the delocalisation of the electron probe. In comparison, these results suggest that scattering cross-sections are most accurately measured by the Gaussian volume approach.

6. StatSTEM software

To facilitate model-based quantitative electron microscopy, a software package has been developed using the MATLAB programming language. A user-friendly graphical user interface has been made to give users a low threshold for advanced model-based quantification. The software is freely available [45] under the GNU public license [24]. A screen shot of the program is given in Fig. 7. The program divides the quantification of electron microscopy image into three sections: preparation, model-based fitting and analysis.

In the preparation part, starting values for the x- and y-coordinates and the pixel size can be defined. Starting coordinates can be inserted by manually selecting peak locations, by using a peak finder routine which looks for local maxima in the image, or by importing a text or MATLAB file containing the coordinates. For complex nanostructures in which different column types are present, atomic columns can be grouped by type.

After the preparation part, the user can fit the Gaussian model by using either model estimation A outlined in subsection 3.1, where a different width for each atomic column is assumed, or model estimation B outlined in subsection 3.2, where the same

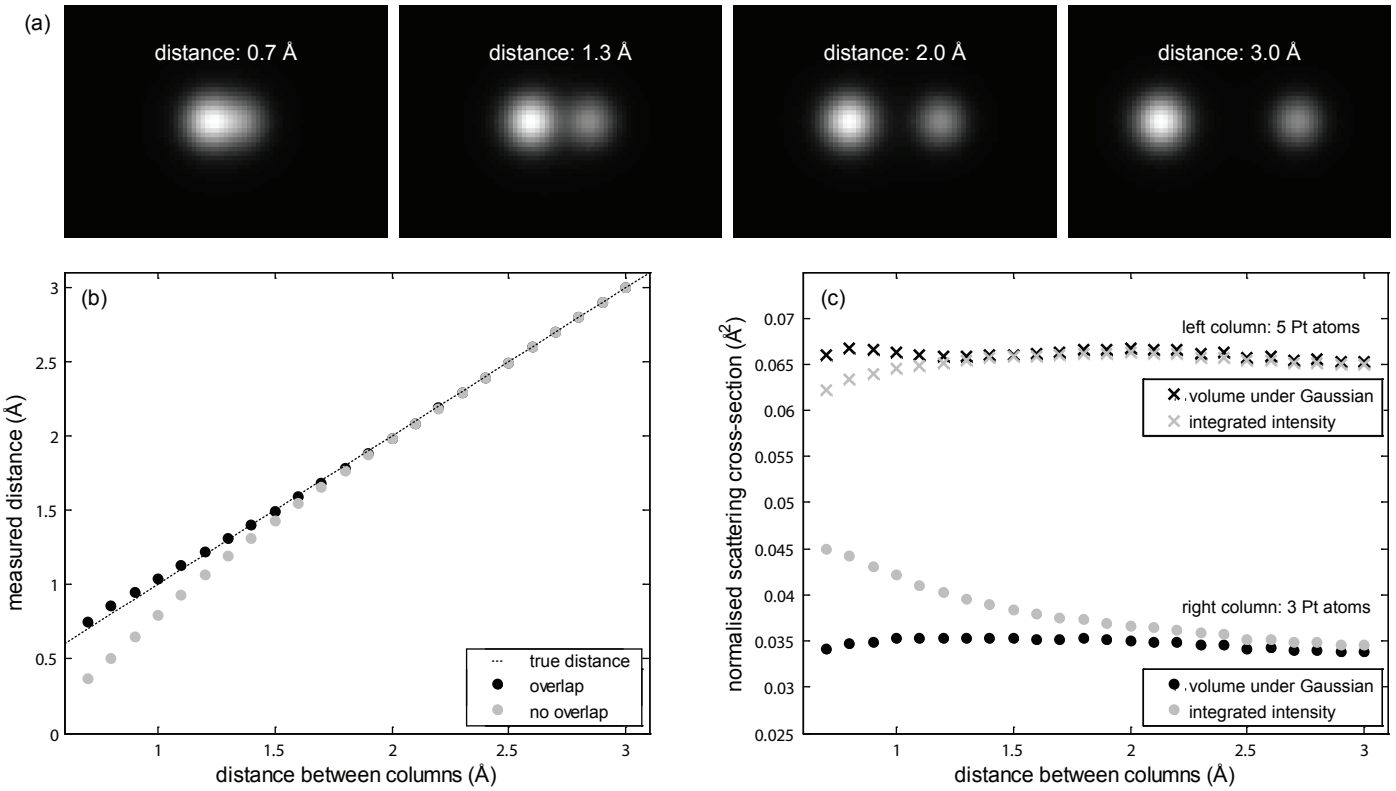

Figure 6: Influence of a neighbouring column on the estimated parameters for different approaches. (a) Examples of simulated images of a 5 and 3 Pt atoms thick column with a varying distance between the columns. (b) The estimated distance between the two columns when taking overlap of column intensities into account and when neglecting the overlap. (c) The normalised scattered intensity estimated by the volumes under the fitted Gaussian function and the integrated intensity obtained from Voronoi cells for the 5 and 3 atoms thick column.

width for each atomic column of the same atomic column type is assumed. Furthermore, the user can predefine the width for each atomic column type in order to estimate only the column positions. For testing the convergence of the model parameters, the option 'fitting under test conditions' is available in which the maximum number of iterations is limited to 4. If the number of columns to be analysed is lower than 100, an algorithm in which all parameters are estimated simultaneously will be used to improve convergence speed. For more columns, the memory consumption may hamper computation and therefore the efficient model estimation algorithm is used. The parallel computing toolbox of MATLAB can be used to further improve the computational speed.

Next, the obtained models and parameters can be used for a further quantitative analysis, for example for atom-counting [18, 19, 21–23]. Here, another set of advanced statistical methods can be employed to count the number of atoms in a single element atomic column. The scattering cross-sections, obtained with the model estimation algorithm, can be presented in the form of a histogram. Owing to a combination of experimental detection noise and residual instabilities, broadened - rather than discrete - components are observed in such a histogram. Therefore, these results cannot directly be interpreted in terms of number of atoms. By evaluation of the so-called integration classification likelihood (ICL) criterion in combination with Gaussian mixture model estimation, the number of components and their respective locations can be found. From the estimated locations of the components, the number of atoms can be quantified. The experimental mean scattering cross-sections (corresponding to the component locations) can independently be compared with the scattering cross-sections resulting from image simulations under the same experimental conditions by loading a library of simulated scattering cross-sections as a function of number of atoms. Details on this method, of which the description is beyond the scope of this paper, can be found in [19, 21]. More detailed information on the StatSTEM package can be found at the website [45].

7. Conclusions

In the present paper, an efficient model-based estimation algorithm has been proposed for the quantification of atomic resolution (S)TEM images in order to analyse large fields of view. The basic idea behind the algorithm is the segmentation of the image into smaller sections containing individual atomic columns for the estimation of the non-linear parameters of the model. This method is much faster than the estimation of all the parameters of the parametric model at the same time, which is a computationally very intensive task.

For this algorithm, the ultimate limits in ADF STEM have been explored. For this purpose, the precision and accuracy of the estimates for the atomic column positions and scattering cross-

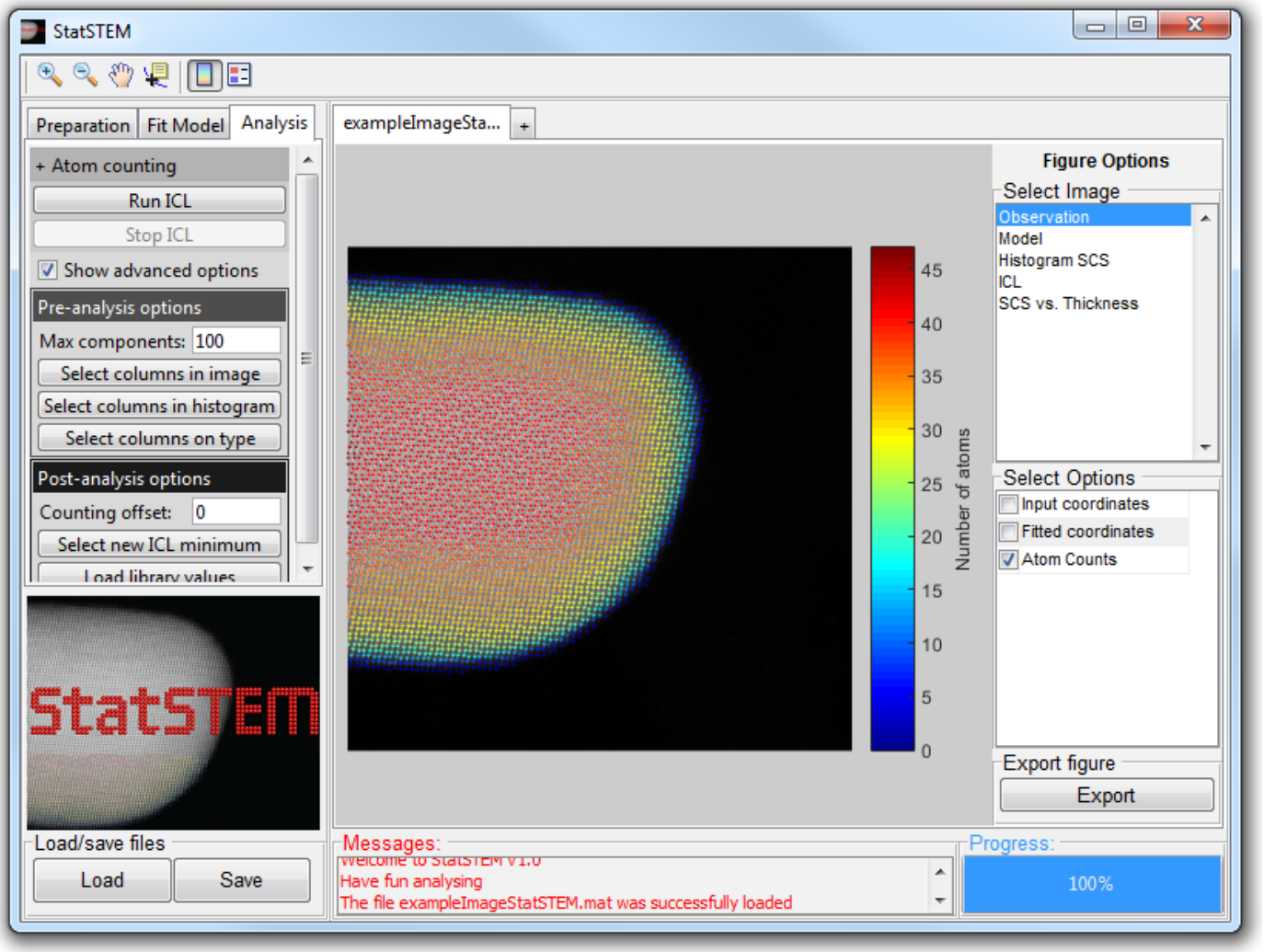

Figure 7: A screen shot of the StatSTEM program, showing the atom counting results on an experimental image of a Pt/Ir nanoparticle

sections have been evaluated using multislice simulations. Although the pixel values of ADF STEM images are modelled as independent Poisson distributed variables, it turns out that even for low incident electron doses, the Cramér-Rao lower bound on the variance of the estimates has been obtained nearly perfectly.

Furthermore, the advantages of a model-based approach have been investigated. This revealed that a model taking overlap into account is essential for estimating unbiasedly the distance between two atomic columns closer than 2 Å. In addition, two different measures for the scattering cross-sections have been compared. The estimated volumes under the Gaussian peak remain constant as a function of the distance between columns, whereas integrated intensities from Voronoi cells cannot take into account overlap between the neighbouring columns, resulting in a bias in the scattering cross-section.

The ideas presented in this paper are combined in a free user friendly program, StatSTEM, to stimulate the use of model-based quantification. The availability of this software will open up new possibilities for quantitative analyses of atomic resolution electron microscopy images.

Acknowledgements

The authors acknowledge financial support from the Research Foundation Flanders (FWO, Belgium) through project fundings (G.0393.11, G.0064.10 and G.0374.13), a Ph.D. research grant to K.H.W. van den Bos, and a postdoctoral research grant to A. De Backer. The research leading to these results has received funding from the European Union Seventh Framework Programme under Grant Agreement 312483 - ESTEEM2 (Integrated Infrastructure Initiative-I3). A. Rosenauer is acknowledged for providing the STEMsim program.

Appendix A. Attainable precision

A thorough description of the Fisher information and the Cramér-Rao lower bound (CRLB) can be found in [35, 46–48]. In this appendix, the Fisher information matrix will be defined and the CRLB will be derived for the atomic column positions

and the scattering cross-sections of ADF STEM images. For such images, the observations are assumed to be statistically independent having a Poisson distribution with the following joint probability function $p(\boldsymbol{\omega})$:

$$p(\boldsymbol{\omega}) = \prod_{k=1}^{K} \prod_{l=1}^{L} \frac{(\lambda_{kl})^{\omega_{kl}}}{\omega_{kl}!} \exp\left(-\lambda_{kl}\right) \tag{A.1}$$

This joint probability function describes the probability that a set of given observations, which are modelled as stochastic variables $\boldsymbol{\omega}$, is equal to $\boldsymbol{\omega}$. The unknown parameters are included through the expectation values λ_{kl} described by a suitable parametric model $f_{kl}(\boldsymbol{\theta})$. This dependence can be expressed as $p(\boldsymbol{\omega};\boldsymbol{\theta})$ and can be used to define a $R \times R$ covariance matrix. This covariance matrix is the so-called Fisher information matrix $F_{\boldsymbol{\theta}}$ and is given by:

$$F_{\boldsymbol{\theta}} = -\mathbb{E}\left[\frac{\partial^2 \ln p(\boldsymbol{\omega};\boldsymbol{\theta})}{\partial \boldsymbol{\theta}^2}\right] \tag{A.2}$$

where $p(\boldsymbol{\omega};\boldsymbol{\theta})$ equals the joint probability function of the stochastic variables $\boldsymbol{\omega}$. The expression between square brackets represents the Hessian matrix of $\ln p(\boldsymbol{\omega};\boldsymbol{\theta})$. The Fisher information is a measure for the physical fluctuation of the observations.

For the observed pixel values in an electron microscopy image, where $p(\boldsymbol{\omega};\boldsymbol{\theta})$ is given by Eq. (A.1), it follows that the (r,s)th element of $F_{\boldsymbol{\theta}}$ equals:

$$F_{rs} = \sum_{k=1}^{K} \sum_{l=1}^{L} \frac{1}{\lambda_{kl}} \frac{\partial \lambda_{kl}}{\partial \theta_r} \frac{\partial \lambda_{kl}}{\partial \theta_s}. \tag{A.3}$$

The diagonal elements of the inverse Fisher information matrix define lower bounds on the parameters $\boldsymbol{\theta}$. This lower bound is independent of the parameters estimation method that is used. In practice, different estimators can be used to estimate the same parameters. However, the variance of unbiased estimators will never be lower than the CRLB. The scattering cross-sections, defined by Eq. (3), are a function of the estimated parameters $\boldsymbol{\theta}$. In order to calculate the CRLB for the scattering cross-sections, the general expression for the CRLB for a function of the model parameters should be used [48]:

$$\sigma^2_{V_n} = \frac{\partial V_n}{\partial \boldsymbol{\theta}} F^{-1}_{\boldsymbol{\theta}} \left(\frac{\partial V_n}{\partial \boldsymbol{\theta}}\right)^T \tag{A.4}$$

where V_n is the scattering cross-section for the nth atomic column in the ADF STEM image. The elements of the Fisher information matrix are given by Eq. (A.3). The vector $\frac{\partial V_n}{\partial \boldsymbol{\theta}}$ is a $(3N + I + 1)$-vector, where N is the total number of columns in the ADF STEM image and I the number of different column types. This vector consists of zeros except for the $(2N+i)$th and $(2N + I + n)$th elements. These elements are equal to:

$$\left[\frac{\partial V_n}{\partial \boldsymbol{\theta}}\right]_{1,2N+i} = \frac{\partial V_n}{\partial \rho_i} = 4\pi\eta_n\rho_i$$

$$\left[\frac{\partial V_n}{\partial \boldsymbol{\theta}}\right]_{1,2N+I+n} = \frac{\partial V_n}{\partial \eta_n} = 2\pi\rho_i^2.$$

Explicit numbers for the CRLB on the variance of the atomic column positions and the scattering cross-sections can be computed by substituting the values of the true parameters into Eqs. (A.3) and (A.4). However, since the observations are Poisson distributed noise realisations of detailed ADF STEM simulations using the STEMsim software [37], only the true parameters of the atomic column positions are available. Therefore, the elements F_{rs} and $\sigma^2_{V_n}$ may only be estimated. This will be done by substituting estimated values for the parameters ρ and η_n for the true parameters. These estimates for the true parameters of ρ and η_n are obtained by fitting the model given by Eq. (7) to the detailed STEMsim model for the ADF STEM image, i.e. in the absence of noise. The estimated Fisher information matrix and estimated lower bounds on the variances will be denoted as $\hat{F}_{\boldsymbol{\theta}}$ and $\hat{\sigma}^2$, respectively.

Appendix B. Confidence intervals on sample mean and sample variance

The $(1-\alpha)\times 100\%$ confidence intervals of the sample mean of the x-coordinate $\bar{\beta}_x$ and the scattering cross-section $\bar{V}$ of the central atom are given by:

$$\left[\bar{\beta}_x - t_{1-\frac{\alpha}{2},N-1}\frac{s_{\beta_x}}{\sqrt{N}}, \bar{\beta}_x + t_{1-\frac{\alpha}{2},N-1}\frac{s_{\beta_x}}{\sqrt{N}}\right] \tag{B.1}$$

$$\left[\bar{V} - t_{1-\frac{\alpha}{2},N-1}\frac{s_V}{\sqrt{N}}, \bar{V} + t_{1-\frac{\alpha}{2},N-1}\frac{s_V}{\sqrt{N}}\right] \tag{B.2}$$

with s_{β_x} and s_V the standard deviation and $t_{1-\frac{\alpha}{2},N-1}$ equals the $1-\frac{\alpha}{2}$ quantile of the Student's t distribution with $N-1$ degrees of freedom, where N equals the sample size, here corresponding to the number of atomic columns.

In order to evaluate the precision of the estimates, the sample variances are compared with the estimated lower bounds on the variances. The $(1-\alpha)\times 100\%$ confidence intervals on the sample variance of the x-coordinate $s^2_{\beta_x}$ and on the sample variance of the scattering cross-section s^2_V are given by:

$$\left[\frac{(N-1)s^2_{\beta_x}}{\chi^2_{\frac{\alpha}{2},N-1}}, \frac{(N-1)s^2_{\beta_x}}{\chi^2_{1-\frac{\alpha}{2},N-1}}\right] \tag{B.3}$$

$$\left[\frac{(N-1)s^2_V}{\chi^2_{\frac{\alpha}{2},N-1}}, \frac{(N-1)s^2_V}{\chi^2_{1-\frac{\alpha}{2},N-1}}\right] \tag{B.4}$$

with $s^2_{\beta_x}$ and s^2_V the sample variances for β_x and V, respectively, and $\chi^2_{1-\frac{\alpha}{2},N-1}$ and $\chi^2_{\frac{\alpha}{2},N-1}$ are the $1-\frac{\alpha}{2}$- and $\frac{\alpha}{2}$-quantiles of the χ^2 distribution with $N-1$ degrees of freedom, respectively.

References

[1] A. J. den Dekker, S. Van Aert, A. van den Bos, D. Van Dyck, Maximum likelihood estimation of structure parameters from high resolution electron microscopy images. Part I: A theoretical framework, Ultramicroscopy 104 (2005) 83–106.

[2] S. Van Aert, A. J. den Dekker, A. van den Bos, D. Van Dyck, J. H. Chen, Maximum likelihood estimation of structure parameters from high resolution electron microscopy images: Part II: A practical example, Ultramicroscopy 104 (2005) 107–125.

[3] D. Van Dyck, High-resolution electron microscopy, Advances in Imaging and Electron Physics 123 (2002) 105–171.

[4] P. D. Nellist, Scanning transmission electron microscopy, in: P. W. Hawkes, J. H. C. Spence (Eds.), Science of Microscopy, Vol. 1, Springer New York, 2007, Ch. 2, pp. 65–132.

[5] S. Bals, S. Van Aert, G. Van Tendeloo, D. Ávila-Brande, Statistical estimation of atomic positions from exit wave reconstruction with a precision in the picometer range, Physical Review Letters 96 (2006) 096106.

[6] L. Houben, A. Thust, K. Urban, Atomic-precision determination of the reconstruction of a 90° tilt boundary in $YBa_2Cu_3O_{7-\delta}$ by aberration corrected HRTEM, Ultramicroscopy 106 (2006) 200–214.

[7] C.-L. Jia, S.-B. Mi, K. Urban, I. Vrejoiu, M. Alexe, D. Hesse, Atomic-scale study of electric dipoles near charged and uncharged domain walls in ferroelectric films, Nature Materials 7 (2008) 57–61.

[8] K. W. Urban, Studying atomic structures by aberration-corrected transmission electron microscopy, Science 321 (2008) 506–510.

[9] S. Van Aert, L. Y. Chang, S. Bals, A. I. Kirkland, G. Van Tendeloo, Effect of amorphous layers on the interpretation of restored exit waves, Ultramicroscopy 109 (2009) 237–246.

[10] A. De Backer, S. Van Aert, D. Van Dyck, High precision measurements of atom column positions using model-based exit wave reconstruction, Ultramicroscopy 111 (2011) 1475–1482.

[11] M. Klingstedt, M. Sundberg, L. Eriksson, S. Haigh, A. Kirkland, G. D., A. De Backer, S. Van Aert, O. Terasaki, Exit wave reconstruction from focal series of HRTEM images, single crystal XRD and total energy studies on Sb_xWO_{3+y} (x 0.11), Z. Kristallogr. 227 (2012) 341–349.

[12] S. Van Aert, W. Van den Broek, P. Goos, D. Van Dyck, Model-based electron microscopy: From images toward precise numbers for unknown structure parameters, Micron 43 (4) (2012) 509 – 515.

[13] M. Huijben, R. G., D. H. A. Blank, S. Bals, S. Van Aert, J. Verbeeck, G. Van Tendeloo, A. Brinkman, H. Hilgenskamp, Electronically coupled complementary interfaces between perovskite band insulators, Nature Materials 5 (2006) 556–560.

[14] K. Kimoto, T. Asaka, X. Yu, T. Nagai, Y. Matsui, K. Ishizuka, Local crystal structure analysis with several picometer precision using scanning transmission electron microscopy, Ultramicroscopy 110 (2010) 778–782.

[15] Y.-M. Kim, J. He, M. D. Biegalski, H. Ambaye, V. Lauter, H. M. Christen, S. T. Pantelides, S. J. Pennycook, S. V. Kalinin, A. Y. Borisevich, Probing oxygen vacancy concentration and homogeneity in solid-oxide fuell-cell cathode materials on the subunit-cell level, Nature Materials 11 (2012) 888–894.

[16] A. B. Yankovich, B. Berkels, W. Dahmen, P. Binev, S. I. Sanchez, S. A. Bradley, A. Li, I. Szlufarska, Voy, Picometre-precision analysis of scanning transmission electron microscopy images of platinum nanocatalysts, Nature Communications 5 (2014) 4155.

[17] S. Van Aert, J. Verbeeck, R. Erni, S. Bals, M. Luysberg, D. Van Dyck, G. Van Tendeloo, Quantitative atomic resolution mapping using high-angle annular dark field scanning transmission electron microscopy, Ultramicroscopy 109 (2009) 1236–1244.

[18] S. Van Aert, K. J. Batenburg, M. D. Rossell, R. Erni, G. Van Tendeloo, Three-dimensional atomic imaging of crystalline nanoparticles, Nature 470 (2011) 374–377.

[19] S. Van Aert, A. De Backer, G. T. Martinez, B. Goris, S. Bals, G. Van Tendeloo, Procedure to count atoms with trustworthy single-atom sensitivity, Physical Review B 87 (064107).

[20] G. T. Martinez, A. Rosenauer, A. De Backer, J. Verbeeck, S. Van Aert, Quantitative composition determination at the atomic level using model-based high-angle annular dark field scanning transmission electron microscopy, Ultramicroscopy 137 (2014) 12–19.

[21] A. De Backer, G. T. Martinez, A. Rosenauer, S. Van Aert, Atom counting in HAADF STEM using a statistical model-based approach: methodology, possibilities, and inherent limitations, Ultramicroscopy 134 (2013) 23–33.

[22] A. De Backer, G. T. Martinez, K. E. MacArthur, L. Jones, A. Béché, P. D. Nellist, S. Van Aert, Dose limited reliability of quantitative annular dark field scanning transmission electron microscopy for nano-particle atom-counting, Ultramicroscopy 151 (2015) 56–61.

[23] S. Van Aert, A. De Backer, G. T. Martinez, A. J. den Dekker, D. Van Dyck, S. Bals, G. Van Tendeloo, Advanced electron crystallography through model-based imaging, IUCrJ 3 (2016) 71–83.

[24] [link].
URL `http://www.gnu.org/licenses/gpl.html`.

[25] B. Goris, A. De Backer, S. Van Aert, S. Gómez-Graña, L. M. Liz-Marzán, G. Van Tendeloo, S. Bals, Three-Dimensional Elemental Mapping at the Atomic Scale in Bimetallic Nanocrystals, Nano Letters 13 (2013) 4236–4241.

[26] B. Goris, J. De Beenhouwer, A. De Backer, D. Zanaga, K. J. Batenburg, A. Sánchez-Iglesias, L. M. Liz-Marzán, S. Van Aert, S. Bals, J. Sijbers, G. Van Tendeloo, Measuring Lattice Strain in Three Dimensions through Electron Microscopy, Nano Letters 15 (10) (2015) 6996–7001.

[27] K. H. W. van den Bos, A. De Backer, G. T. Martinez, N. Winckelmans, S. Bals, P. D. Nellist, S. Van Aert, Unscrambling mixed elements using high angle annular dark field scanning transmission electron microscopy, Physical Review Letters, accepted.

[28] A. Rosenauer, T. Mehrtens, K. Müller, K. Gries, M. Schowalter, P. V. Satyam, S. Bley, C. Tessarek, D. Hommel, K. Sebald, M. Seyfried, J. Gutowski, A. Avramescu, K. Engl, S. Lutgen, Composition mapping in InGaN by scanning transmission electron microscopy, Ultramicroscopy 111 (2011) 1316–1327.

[29] T. Mehrtens, M. Schowalter, D. Tytko, P. Choi, D. Raabe, L. Hoffmann, H. Jonen, U. Rossow, A. Hangleiter, A. Rosenauer, Measurement of the indium concentration in high indium content ingan layers by scanning transmission electron microscopy and atom probe tomography, Applied Physics Letters 102 (2013) 132112.

[30] H. E, K. E. MacArthur, T. J. Pennycook, E. Okunishi, A. J. D'Alfonso, N. R. Lugg, L. J. Allen, P. D. a. Nellist, Probe integrated scattering cross sections in the analysis of atomic resolution HAADF STEM images, Ultramicroscopy 133 (2013) 109–119.

[31] L. Jones, K. E. MacArthur, V. T. Fauske, A. T. J. van Helvoort, P. D. Nellist, Rapid Estimation of Catalyst Nanoparticle Morphology and Atomic-Coordination by High-Resolution Z-Contrast Electron Microscopy, Nano Letters 14 (11) (2014) 6336–6341.

[32] A. J. den Dekker, J. Gonnissen, A. De Backer, J. Sijbers, S. Van Aert, Estimation of unknown structure parameters from high-resolution (s)tem images: What are the limits?, Ultramicroscopy 134 (2013) 34–43.

[33] W. H. Lawton, E. A. Sylvestre, Elimination of Linear Parameters in Nonlinear Regression, Technometrics 13 (3) (1971) 461–467.

[34] J. C. Lagarias, J. A. Reeds, M. H. Wright, P. E. Wright, Convergence Properties of the Nelder-Mead Simplex Method in Low Dimension, SIAM Journal of Optimization 9 (1) (1998) 112–147.

[35] A. van den Bos, A. J. den Dekker, Resolution reconsidered - conventional approaches and an alternative, Advances in Imaging and Electron Physics 117 (2001) 241–360, san Diego: Academic Press.

[36] K. Ishizuka, A practical approach for STEM image simulation based on the FFT multislice method, Ultramicroscopy 90 (2002) 71–83.

[37] A. Rosenauer, M. Schowalter, STEMSIM - a New Software Tool for Simulation of STEM HAADF Z-Contrast Imaging, in: A. Cullis, P. Midgley (Eds.), Microscopy of Semiconducting Materials 2007, Vol. 120 of Springer Proceedings in Physics, Springer Netherlands, 2008, pp. 170–172.

[38] A. Rosenauer, K. Gries, K. Müller, A. Pretorius, M. Schowalter, A. Avramescu, K. Engl, S. Lutgen, Measurement of specimen thickness and composition in $Al_xGa_{1-x}N$/GaN using high-angle annular dark field images, Ultramicroscopy 109 (2009) 1171–1182.

[39] H. X. Gao, L.-M. Peng, Parameterization of the temperature dependence of the Debye-Waller factors, Acta Crystallographica A 55 (1999) 926–932.

[40] J. P. Buban, Q. Ramasse, B. Gipson, N. D. Browning, H. Stahlberg, High-resolution low-dose scanning transmission electron microscopy, Journal of Electron Microscopy 59 (2010) 103–112.

[41] L. Jones, P. D. Nellist, Identifying and Correcting Scan Noise and Drift in the Scanning Transmission Electron Microscope, Microscopy and Microanalysis 19 (2013) 1050–1060.

[42] S. M. Anthony, S. Granick, Image Analysis with Rapid and Accurate Two-Dimensional Gaussian Fitting, Langmuir 25 (2009) 8152–8160.

[43] Y. Wang, U. Salzberger, W. Sigle, E. Suyolcu, P. A. van Aken, Oxygen octahedra picker: A software tool to extract quantitative information from STEM images, Ultramicroscopy 168 (2016) 46–52.

[44] A. De Backer, A. De wael, J. Gonnissen, S. Van Aert, Optimal experimental design for nano-particle atom-counting from high-resolution STEM images, Ultramicroscopy 151 (2015) 46–55.
[45] [link].
URL https://github.com/quantitativeTEM/StatSTEM
[46] A. van den Bos, Handbook of Measurement Science, Vol. 1, Chicester Wiley, 1982, Ch. Parameter estimation, pp. 331–377.
[47] B. R. Frieden (Ed.), Physics from Fisher Information - A Unification, Cambridge University Press, Cambridge, 1998.
[48] A. van den Bos, Parameter estimation for scientists and engineers, Wiley, 2007.